International Journal of Heat and Mass Transfer 55 (2012) 5673–5686

Contents lists available at SciVerse ScienceDirect

International Journal of Heat and Mass Transfer

journal homepage: www.elsevier.com/locate/ijhmt

Nanofluid stabilizes and enhances convective boiling heat transfer in a single microchannel

Li Xu [a], Jinliang Xu [a,b,*]

[a] State Key Laboratory of Alternate Electrical Power System with Renewable Energy Sources, North China Electric Power University, Beijing 102206, PR China
[b] The Key Laboratory of New and Renewable Energy, School of Renewable Energy, North China Electric Power University, Beijing 102206, PR China

ARTICLE INFO

Article history:
Received 21 June 2011
Received in revised form 11 May 2012
Accepted 15 May 2012
Available online 21 June 2012

Keywords:
Nanofluid
Boiling
Heat transfer
Flow instability

ABSTRACT

The flow boiling heat transfer in a single microchannel was investigated with pure water and nanofluid as the working fluids. The microchannel had a size of 7500 × 100 × 250 μm, which was formed by two pyrex glasses and a silicon wafer. A platinum film with a length of 3500 μm and a width of 80 μm was deposited at the bottom channel surface, acting as the heater and temperature sensor. The nanofluid had a low weight concentration of 0.2%, consisting of de-ionized water and 40 nm Al_2O_3 nanoparticles. The nanoparticle deposition phenomenon was not observed. The boiling flow displays chaotic behavior due to the random bubble coalescence and breakup in the milliseconds timescale at moderate heat fluxes for pure water. The flow instability with large oscillation amplitudes and long cycle periods was observed with further increases in heat fluxes. The flow patterns are switched between the elongated bubbles and isolated miniature bubbles in the timescale of 100 s. It is found that nanofluid significantly mitigate the flow instability without nanoparticle deposition effect. The boiling flow is always stable or quasi-stable with significantly reduced pressure drop and enhanced heat transfer. Miniature bubbles are the major flow pattern in the microchannel. Elongated bubbles temporarily appear in the milliseconds timescale but isolated miniature bubbles will occupy the channel shortly. The decreased surface tension force acting on the bubble accounts for the smaller bubble size before the bubble departure. The inhibition of the dry patch development by the structural disjoining pressure, and the enlarged percentage of liquid film evaporation heat transfer region with nanoparticles, may account for the heat transfer enhancement compared to pure water.

1. Introduction

Nanofluid is a base fluid containing nanoparticles, which has been received great attention since the concept was proposed by Choi [1]. Applications in heat transfer devices are due to its higher thermal conductivities compared to pure liquid. Several investigators reported the thermal conductivity enhancement of nanofluid with low volume concentration (1–5%) to be more than 20% [2–4]. Eastman et al. [5] reported an outstanding increase in thermal conductivity of 40% with only 0.3% volume concentration of copper nanoparticles having an average size of less than 10 nm.

The flow boiling of nanofluid was studied by Kim et al. [6,7] in a circular tube using electrical heating. The critical heat flux (CHF) was significantly increased with nanofluid containing alumina, diamond, and zinc oxide particles. They also found that at higher nanofluid concentrations, the CHF enhancement was higher and the static contact angle on the fouled surface was lower. Ahn et al. [8] performed flow boiling experiments of nanofluid. They concluded that the CHF enhancement ratio ($CHF_{nanofluid}/CHF_{purewater}$) at a given flow velocity was related to the wettability due to the nanoparticles deposition on the heater surface. Although the CHF increased in the ad-hoc tests, the enhancement ratio ($CHF_{nanoparticles\text{-}coated}/CHF_{purewater}$) at a given flow velocity was less than that observed for nanofluid, supporting the conclusion that the nanoparticles deposited on the wall surface has an effect on the flow boiling.

The heat transfer coefficient can be decreased, unaffected, or increased for nucleate boiling of nanofluid. Das et al. [9] conducted boiling heat transfer studies of nanofluid, boiled Al_2O_3 nanofluid on a standard and a roughened cartridge heater. They identified the heat transfer deterioration by the fouled heater surface. Kim et al. [6,7] noted that the change of boiling heat transfer coefficient and CHF could be attributed to the surface deposition effects of nanoparticles. A thin deposition layer on the heater surface altered the active nucleation sites and introduced an additional thermal resistance. Kwark et al. [10] reported the nanoparticles-coated heater effects for pool boiling. The varied coating layer thickness and

* Corresponding author at: State Key Laboratory of Alternate Electrical Power System with Renewable Energy Sources, North China Electric Power University, Beijing 102206, PR China. Tel.: +86 10 61772268.
E-mail address: xjl@ncepu.edu.cn (J. Xu).

0017-9310/$ - see front matter © 2012 Elsevier Ltd. All rights reserved.
http://dx.doi.org/10.1016/j.ijheatmasstransfer.2012.05.063

Nomenclature

A	heater area, m^2
D	bubble diameter, m
D_b	bubble depart diameter, m
$\boldsymbol{F}_g$	buoyant force, N
$\boldsymbol{F}_\sigma$	surface tension force, N
g	acceleration due to gravity, m/s^2
h	heat transfer coefficient, W/m^2K
I	electric current, A
M	mass flow rate, kg/s
p	pressure, Pa
q	effective heat flux, W/cm^2
ΔT	temperature difference, °C
V_2	voltages in the precision resistance, V
Y	vertical coordinate, m
C_p	specific heat, J/(kgK)
D_B	diameter of the dry zone, m
$\boldsymbol{F}_d$	drag force, N
$\boldsymbol{F}_l$	inertial force, N
G	mass flux, kg/m^2s
H	liquid film thickness, m
h_{lv}	latent heat of evaporation, kJ/kg
k	thermal conductivity, W/mK
ΔP	pressure drop, Pa
Q	heating power, W
R	precision resistance, Ω
V_1	voltages in the microheater, V
X	horizontal coordinate, m

Greek symbols

$\Delta\rho$	density difference between liquid and vapor, kg/m^3
$\Pi(h)$	disjoining pressure of a film, Pa
σ	interfacial tension, N/m
μ	viscosity, Pa · s
θ	contact angle, °
ρ	density, kg/m^3
Φ	volume concentration, %

Subscripts

ave	average value
film	Pt film
l	liquid
np	nanoparticle
pw	pure water
v	vapour
f	working fluid
in	inlet
nf	nanofluid
out	outlet
sat	saturation temperature

structures were created by changing the nanofluid boiling parameters, including the heat flux, boiling duration and nanoparticles concentration. They focused on the pool boiling heat transfer of nanofluid. The forced convection boiling heat transfer of nanofluid should be different from the pool boiling heat transfer of nanofluid. Ahn et al. [11] studied water boiling on a nanoparticles-coated heater at flow velocities ranging from 0 to 0.4 m/s, and assessed the boiling heat transfer performance. Different wetting zones on bare and nanoparticles coated heaters were observed.

Lee and Mudawar [12] noted that boiling of nanofluid could cause failure by forming large clusters near the channel exit due to localized evaporation once boiling was commenced. This and other practical disadvantages bring into question of the overall merit of using nanofluid in microchannel heat sinks. Peng et al. [13] investigated the flow boiling heat transfer of refrigerant-based nanofluid, the flow boiling in a smooth tube at different nanoparticle concentrations, mass fluxes, heat fluxes and inlet vapor qualities. An increase of the boiling heat transfer coefficient by a maximum of 29.7% was identified, caused by the boundary layer height reduction from the nanoparticle disturbances and a molecular adsorption layer formation on the tube surface. The coating layer of nanoparticles was not observed in their studies. Henderson et al. [14] dispersed the nanoparticles in refrigerants and quantified the effects of nanoparticles on the heat transfer of R134a and R13a/POE mixtures. A decrease in the boiling heat transfer was found with increases in particle concentrations over the tested parameter ranges. There was a little change of the heat transfer coefficients when the R134a/POE/CuO nanofluid with a volume fraction of 0.02% was used. However, the heat transfer coefficients of the R134a/POE/CuO nanofluid could be increased by 52% and 76% for volume fractions of 0.04% and 0.08%.

The motivation of this work is to study effect of nanofluid on the boiling heat transfer in a single microchannel. The test section was fabricated by microelectromechanicalsystem (MEMS) technique, ensuring precise geometry parameters. A thin platinum film of 500 nm was deposited at the channel bottom surface, acting as the heater and temperature sensor. Such hardware ensured direct heat transfer between heater surface and fluid. Comparisons were made with and without nanoparticles, case by case. It was found that nanofluid could not only significantly enhance heat transfer, but also decrease pressure drops across the microchannel. Besides, the boiling heat transfer of nanofluid became stable or quasi-stable. Physical explanation of the observed phenomena was given. Some of the experimental findings reported here were not reported previously.

2. Description of the experiment

2.1. The nanofluids and physical properties

The γ-Al_2O_3 nanoparticles had quasi-spheric shape with an average diameter of 40 nm. The nanoparticles were dispersed in de-ionized water by ultrasonic oscillation method. The weight concentration was 0.2%, corresponding to the volume fraction of 0.052%, which was lower than those used in the literature [9,12]. The dispersant fluid was not used due to the low particle concentration. Fig. 1 shows the nanoparticles photo. Table 1 gave the physical properties of pure water and nanofluid of 0.2% weight concentration at atmospheric pressure and 25 °C.

Physical properties of the nanofluid are computed based on the following equations [2–4].

$$\rho_{nf} = \phi\rho_{np} + (1-\phi)\rho_{pw} \tag{1}$$

$$C_{p,nf} = \phi C_{p,np} + (1-\phi)C_{p,pw} \tag{2}$$

$$\mu_{nf} = (1+2.5\phi)\mu_{pw} \tag{3}$$

$$k_{nf} = \frac{k_{np} + 2k_{pw} - 2\phi(k_{pw}-k_{np})}{\frac{k_{np}}{k_{pw}} + 2 + \phi\left(\frac{k_{pw}-k_{np}}{k_{pw}}\right)} \tag{4}$$

Because physical properties of nanofluid are important for heat transfer analysis, we also measured the density, specific heat, viscosity and thermal conductivity with high accuracy instruments.

(a) the prepared nanofluid

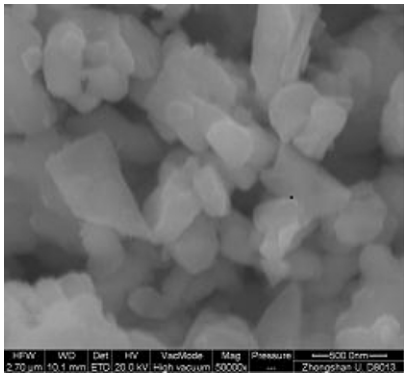

(b) SEM images of nanoparticles

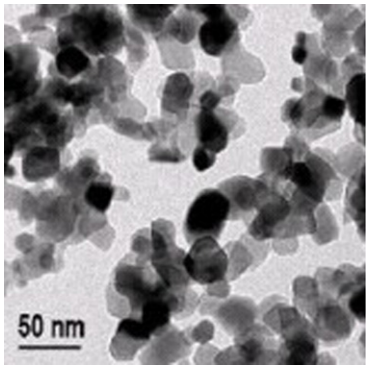

(c)TEM images of nanofluids

Fig. 1. The prepared nanofluid and the enlarged nanoparticles.

Table 1
Major physical properties of pure water and nanofluid of 0.2% weight concentration at atmospheric pressure and 25 °C.

Fluid	ρ_p (kg/m^3)	C_p (J/kgK)	μ_p (Pa · s)	k_p (W/mK)
Pure water (*pw*)	1027	4194	9.11×10^{-4}	0.607
Nanofluid (*nf*, computed)	1031	4189	9.14×10^{-4}	0.609
Nanofluid (*nf*, measured)	1030	4192	9.18×10^{-4}	0.608

Table 1 shows these parameters, with the difference between the computed and measured values smaller than 0.5%, which are accurate enough to perform the heat transfer analysis.

2.2. Microchannel test section and experimental setup

Fig. 2 shows the microchannel test section, consisting of three pieces bonded together. The top and bottom pieces were the two 7740 Pyrex glasses, each having a thickness of 400 μm. The central part was a silicon wafer having a thickness of 250 μm. A channel with a length of 7500 μm and a width of 100 μm was etched in the silicon substrate. The single channel was between the inlet and outlet ports (see Fig. 2b). A thin platinum film of 500 nm thickness was deposited at the top surface of the bottom Pyrex glass by the sputtering process. The film thickness variance of less than 10 nm was detected by an electrical probe. The film had a size of 3500×80 μm for the heater and temperature sensor (see Fig. 2c). Two gold pads were connected with the heater as the electrodes. The design shown in Fig. 2 ensured a direct heat transfer between the thin film heater and the fluid in the microchannel. The thermal response was fast due to the ultra-small mass of the film heater. The thermal efficiency was defined as the heat received by the fluid divided by the heating power. Because the Pyrex glass had significantly low thermal conductivity, the system thermal efficiency was in the range of 0.92–0.95. Besides, the thin film heater had excellent linear relationship between the resistance and temperature (see Fig. 3). Thus it was also regarded as the temperature sensor to measure temperatures during heat transfer in the microchannel.

An open forced convection loop was built to perform the experiment (see Fig. 4). The flow rate of pure water or nanofluid was provided by a syringe pump. Before the nanofluid entered the test section, a constant temperature bath adjusted the fluid to a target temperature. A 2 μm filter prevented large solid particles entering the test section. Because the pore size of the filter was 50 times larger than the nanoparticle size, the filter had no effect on the nanofluid concentration in the microchannel. A pressure drop sensor was arranged across the test section. Two thermocouples were arranged at the inlet and outlet of the test section to measure the fluid temperatures. The fluid at the microchannel outlet was condensed in a capillary tube and finally collected in a glass beaker. The film heater at the microchannel bottom surface was driven by a DC power supply circuit, in which a precise resistance R was included. As shown in Fig. 4, the transient voltage V_1 was applied on the film heater, and V_2 was applied on the resistance R.

An optical system includes a microscope and a high speed camera (HG-100 K, Redlake Inc., USA) with high speed recording rate of 20,000 fps, measuring the transient bubble behavior in the microchannel. A high speed data acquisition system (DL750, Yokogawa Inc., Japan) measured the signals of V_1 and V_2. The optical measurement system and the high speed data acquisition system were synchronized by a synchronization hub, with the time resolution of 10 ns. The present study used the data sampling rate in the range of 100–1000 samples per second, corresponding to the time interval of data sampling in the range of 1–10 ms. All the parameters were measured with the synchronization time of 10 ns, which was significantly shorter than the time interval of the data sampling.

2.3. Data reduction and uncertainty analysis

By measuring the two voltages of V_1 and V_2 (see Fig. 4), the heater resistance during flow and heat transfer process is calculated as

$$R_{film} = \frac{V_1}{V_2} R - R_{Au1} - R_{Au2} \tag{5}$$

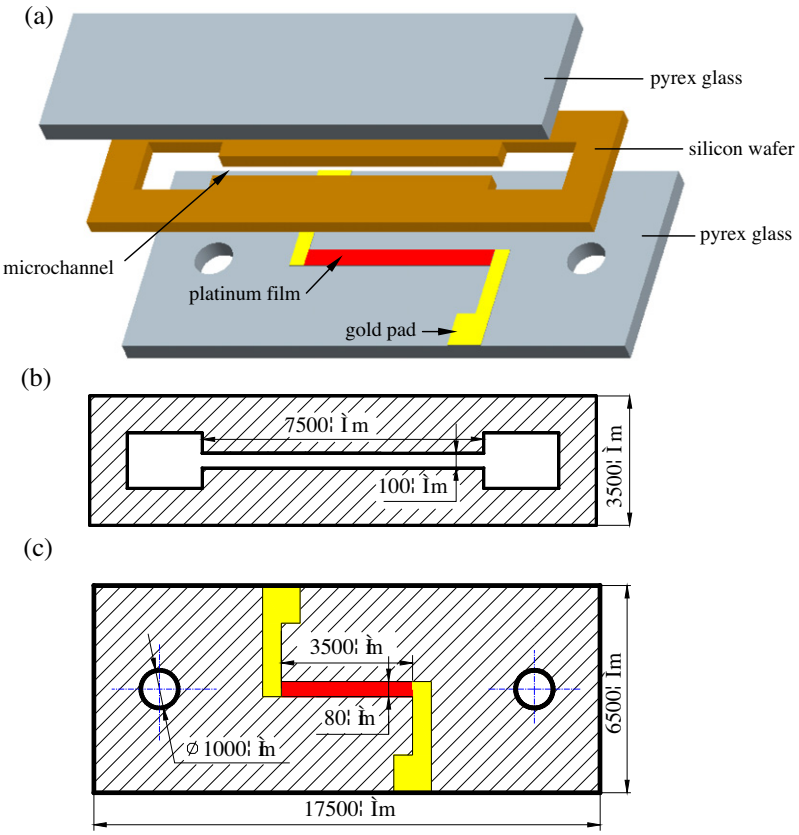

Fig. 2. The microchannel test section, (a) the three pieces of the elements, (b) the top view of the center silicon microchannel, (c) the deposited platinum film on the bottom pyrex glass surface.

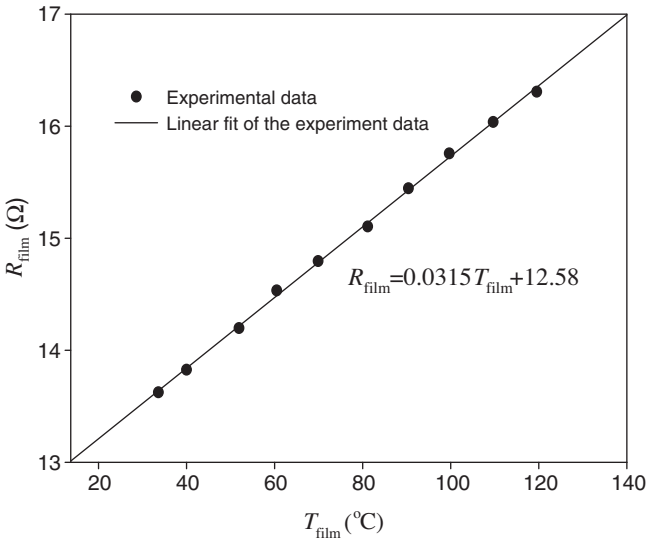

Fig. 3. The calibrated heater resistance versus temperature.

where R is the known resistance which is selected from a precise resistance box and R_{Au1} and R_{Au2} are the two gold pad resistances, respectively. Using the linear curve fit shown in Fig. 3, the film heater temperature can be easily computed.

The Joule heating power on the thin film heater was calculated as

$$Q = I_{film}^2 R_{film} = \left(\frac{V_2}{R}\right)^2 \left(\frac{V_1}{V_2}R - R_{Au1} - R_{Au2}\right) \quad (6)$$

The heat flux on the film heater surface is

$$q_{film} = Q/A \quad (7)$$

where A is the film heater area by 3500 × 80 μm.

Considering the heat loss of the heat transfer system to the environment, the effective heat received by the fluid in the microchannel is

$$q = q_{film} - q_{loss} \quad (8)$$

It is noted that q is the transient heat flux on the heater surface, which is different from q_{ave} (the time averaged heat flux on the heater surface), $q_{ave} = \int_0^\tau q dt/\tau$, where τ is the measurement time involved in the integration.

An initial test was performed to estimate the heat dissipated to the environment when the heater was powered on and the microchannel was empty. An applied heating power corresponds to a specific heater temperature. A linear relationship can be obtained as

$$q_{loss} = a \times T_{film} + b \quad (9)$$

Physically, Eq. (9) reflects the natural convection heat transfer of the test chip to the air environment, with the parameter a indicating the combined effect of the natural convection heat transfer coefficient and the chip surface area exposed in the air environment, b indicating the combined effect of the natural convection heat transfer coefficient and the environment temperature. Under the laboratory test condition with neglectable air convection effect and the environment temperature variation of 1 °C, the experimentally determined parameters were a = 2.97 and b = −93.50, yielding the uncertainty of q_{loss} of 3.9%.

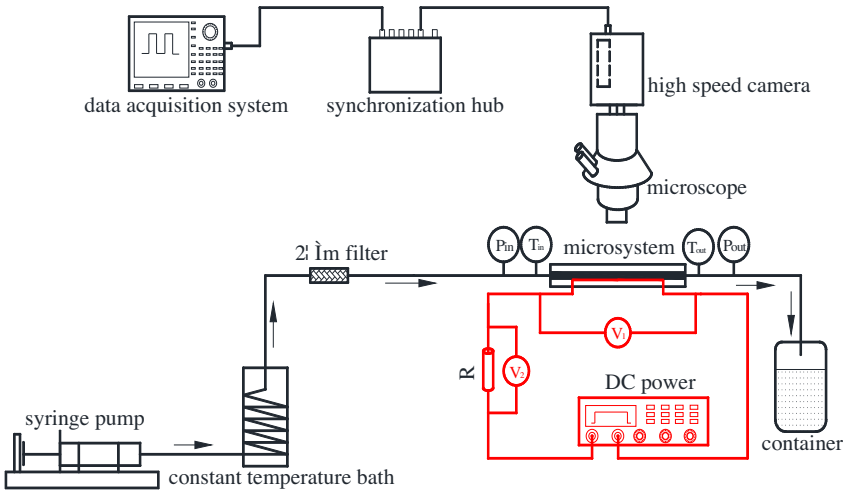

Fig. 4. The forced convection loop and measurement system.

Table 2
The parameter uncertainties or relative error.

Parameter	Explanation	Uncertainty or relative error
G	Mass flux, kg/m^{2}s	0.5%
h	Heat transfer coefficient, W/m^{2}K	4.6%
P_{in} and P_{out}	Inlet/outlet pressure, Pa	0.1%
q	Heat flux, W/cm^2	4.3%
R	Precision resistance, Ω	0.01Ω
T_{in} and T_{out}	Inlet and outlet Temperature, °C	0.3 °C
T_{film}	Heating film Temperature, °C	1.7 °C
T_{sat}	Saturation temperature, °C	0.2 °C
V_1 and V_1	Voltage, V	0.1 mV

The present work acquires the average heat transfer coefficient over the whole heater surface, noting that the heat transfer coefficient can be varied versus time:

$$h_{ave} = q/\Delta T \tag{10}$$

where ΔT is the temperature difference between the film heater and the fluid, i.e., $\Delta T = T_{film} - T_f$, where T_f is the fluid temperature, which is the average of the inlet and outlet of fluid temperatures, $T_f = (T_{in} + T_{out})/2$. For the present experiment, T_{in} was at the room temperature (about 20–27 °C), and T_{out} was the saturation temperature at the atmospheric pressure (about 100 °C). Thus the temperature difference between inlet and out was about 73–80 °C.

We estimated the uncertainties of various parameters involved in this experiment. According to Holman [15], If R is a given function of the independent variables of $x_1, x_2, x_3, \ldots, x_n$, $R = R(x_1, x_2, x_3, \ldots, x_n)$, and $\Delta x_1, \Delta x_2, \Delta x_3, \ldots, \Delta x_n$ are the uncertainties in these independent variables, the uncertainty of R can be evaluated by:

$$\Delta R = \sqrt{\left(\frac{\partial R}{\partial x_1}\Delta x_1\right)^2 + \left(\frac{\partial R}{\partial x_2}\Delta x_2\right)^2 + \cdots + \left(\frac{\partial R}{\partial x_n}\Delta x_n\right)^2} \tag{11}$$

Table 2 shows the parameter uncertainties or relative errors.

3. Results and discussion

3.1. Description of the flow and heat transfer with and without nanoparticles

The present work covers the following data ranges: effective heat fluxes on the film heater (q) of 0–1000 W/cm^2, mass fluxes (G) of 171, 285 and 401 kg/m^{2}s. Due to the small heater surface used, the heat fluxes are significantly large than those reported in the literature [16–18]. Besides, the present heating method ensures temperature recordings with the accuracy of 1.7 °C and the response time of 1 ms. Figs. 5 and 6 show pressure drops and surface superheats versus heat fluxes. In order to consider the nanofluid effect on the heat transfer, three typical cases are demonstrated, with almost identical mass fluxes for pure water and nanofluid in each comparative case.

Fig. 5a shows pressure drops versus heat fluxes, in which the pressure drop was averaged over time. Three groups of curves were compared with each other for pure water and nanofluid. Pressure drops of pure water have a transition point, beyond which the pressure drops are increased sharply, i.e., pressure drops are much larger once boiling is triggered than those for the single-phase liquid flow. This phenomenon is observed in many other studies. This is not true for nanofluid. Instead, pressure drops show a slight parabola shape with continuous increases in heat fluxes. Curves of $\Delta p \sim q_{ave}$ are crossed over for the two working fluids, i.e., pressure drops are slightly larger in the single-phase liquid flow region, but they are significantly smaller in the boiling flow region, for nanofluid compared to pure water.

Fig. 5b–d identifies pressure drops versus heat fluxes, but pressure drops are not plotted by the time averaged values. The OFI (Onset of Flow Instability) can be identified as the minimum point in the $\Delta p \sim G$ curve with a given heat flux, which is very close to the boiling incipience point for microchannel flow [17,18]. Alternatively, the OFI point takes place within a short distance downstream of the transition point of the $\Delta p \sim q_{ave}$ curve, beyond which the flow displays the flow instability. The top and bottom margins of the error bars in Fig. 5 are the maximum and minimum pressure drop values during the oscillation. The range of the error bars is the oscillation amplitude for the unsteady flow. The unstable boiling flow in microchannels was also observed by many other investigators [16–18]. It is found that nanofluid mitigates the boiling flow instability, which will be explained later.

Fig. 6 shows the heater surface superheats against heat fluxes. The heater surface superheats are smaller, indicating the heat transfer enhancement in both liquid flow and boiling flow regions for nanofluid than those for pure water. Very large oscillation amplitudes of surface superheats are observed for pure water, which attain more than 100 °C in Fig. 6b–d, but neglectable oscillation amplitude is identified for nanofluid. The smaller heater surface temperature for nanofluid is due to the enhanced heat transfer coefficient compared to pure water. The reason will be discussed in Section 3.5. Due to the flow pattern transition between elongated bubbles and miniature bubbles, the heater temperatures are varied due to the variation of the heat transfer coefficients caused by the

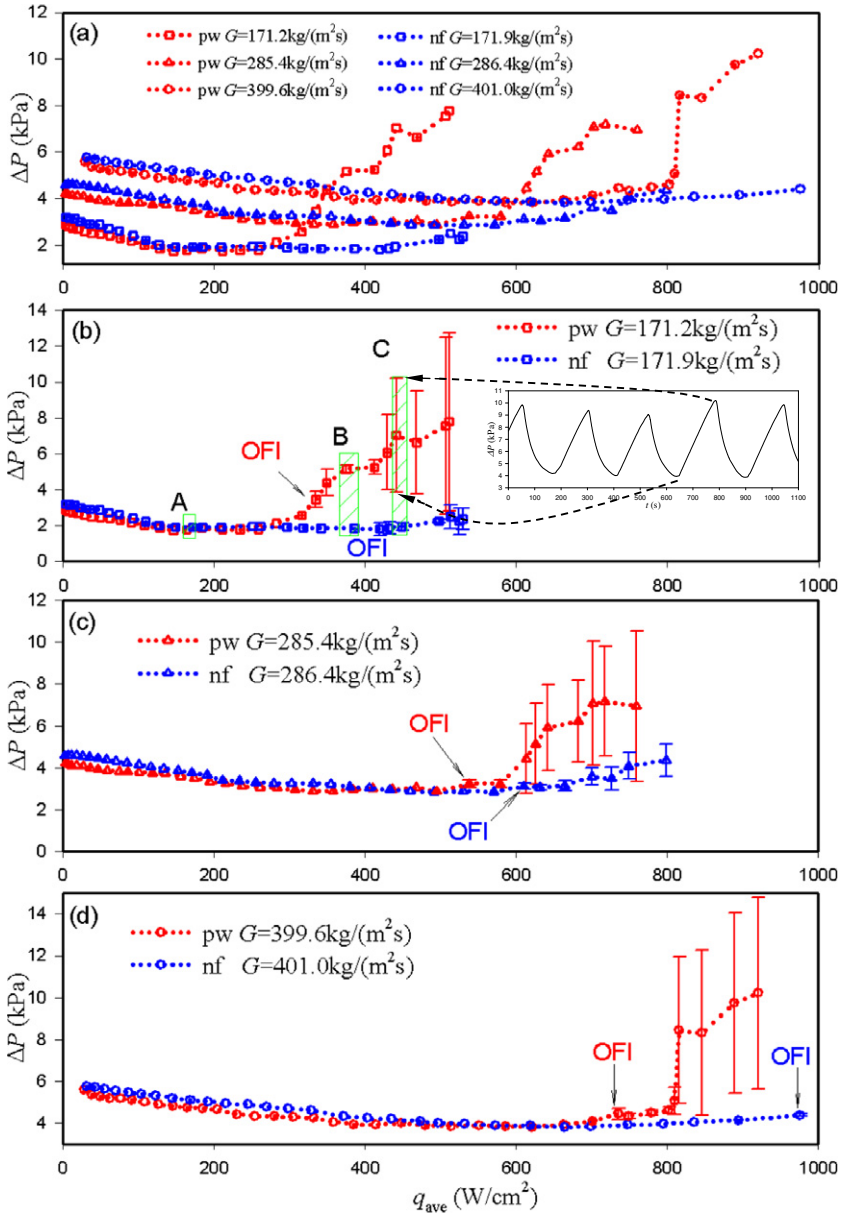

Fig. 5. Pressure drops versus heat fluxes on the film heater surface at the three groups of mass fluxes (T_{in} = 27 °C).

flow pattern transition for pure water. However, the boiling flow is stable without apparent flow pattern transition for nanofluid, thus the heater temperatures do not change versus time. In Figs. 5b and 6b, we select three specific points of A, B and C. The point A refers to the single-phase liquid flow for both nanofluid and pure water. The point B is just after the OFI point for pure water, but the OFI point is not reached for nanofluid. The bubble size is larger once boiling is triggered, causing larger flow disturbance for pure water. Thus the OFI point takes place earlier for pure water than that for nanofluid. The point C has large oscillation amplitude for pure water, but has neglectable oscillation amplitude for nanofluid.

3.2. Single-phase liquid flow and heat transfer with and without nanoparticles

Based on Figs. 5 and 6, the running parameters are almost identical for pure water and nanofluid at point A. The heat flux and mass flux are 166 W/cm^2 and 171.2 kg/m^{2}s for pure water, they are 168 W/cm^2 and 171.9 kg/m^{2}s for nanofluid. The heat flux difference for the two working fluids is 2%. Fig. 7 gave various parameters versus time. It is seen that these parameters are quite stable. However, the pressure drop for nanofluid is about 10% higher than that for pure water. The heater surface temperature for nanofluid is about 10% lower than that for pure water. The heat transfer coefficient for nanofluid is about 17% higher than that for pure water, indicating the heat transfer enhancement for single-phase forced convection heat transfer with nanofluid, which is consistent with available studies [2–4].

3.3. Unstable boiling for pure water and quasi-stable boiling for nanofluid at the point B

The point B in Figs. 5 and 6 has the mass flux of 171 kg/m^{2}s and heat fluxes of 370–385 W/cm^2 for pure water and nanofluid. The difference of heat fluxes for the two working fluids is about 3%. Fig. 8 shows various parameters versus time, showing chaotic behavior for pure water and quasi-stable for nanofluid. The pressure drop is about 1.8 kPa for nanofluid, significantly lower than

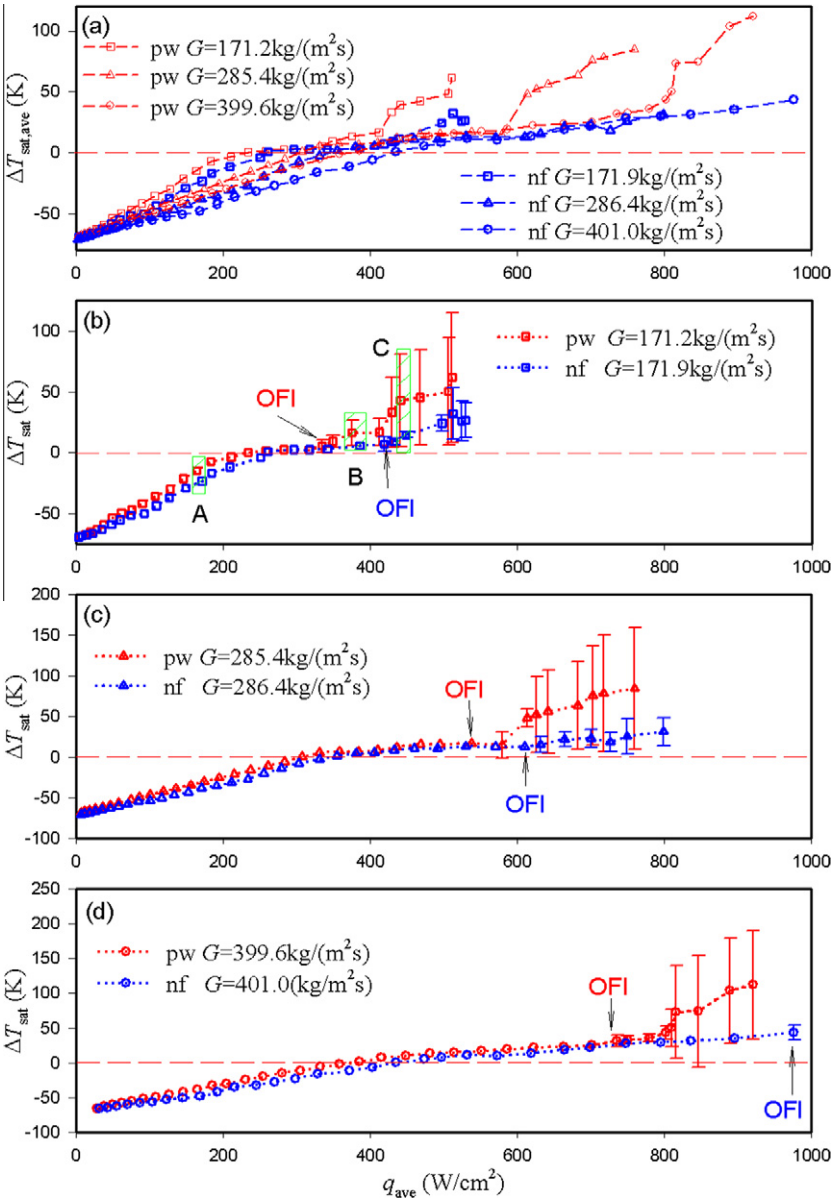

Fig. 6. The film heater surface temperatures versus its heat fluxes at the three groups of mass fluxes (T_{in} = 27 °C).

5.2 kPa for pure water. There is no apparent change of pressure drops for the initial experiment and that after three days operation. The difference is very small and almost covers in the transducer error range. The objective of choosing 3 days gap is to demonstrate no particle deposition on the heater surface. The nanofluid for use after three days operation was prepared three days ago.

The oscillation amplitude of the heater surface temperatures attains more than 15 °C for pure water. Because the temperature difference between the heater surface temperature and fluid is small, the heat transfer coefficient is sensitive to the temperature difference. The oscillation amplitude of the heat transfer coefficient attains more than 100 kW/m^{2}K for pure water, with the maximum value reaching 200 kW/m^{2}K. The heater surface temperature is lower and the heat transfer coefficient is larger for nanofluid than those for pure water.

Fig. 9 shows the flow pattern in the microchannel for pure water. There are four bubbles in the microchannel at time *t*. Because the channel has a width of 100 μm and a depth of 250 μm, the bubbles are confined in the channel width direction, noting that the heater surface is hydrophilic. The moving speeds of these bubbles are different due to their uneven expansion. The distance between two neighboring bubbles is short at t + 2.8 ms and t + 3.0 ms. The two central bubbles are merged to form an elongated bubble at t + 3.4 ms, thus there are three bubbles at such time. Further coalescence of bubbles forms two elongated bubbles at t + 42.2 ms. However, breakup of the elongated bubble can take place. The strong evaporation at the heater surface causes the vapor expansion locally, separating an elongated bubble into two bubbles. Thus the number of bubbles turns to be four again at t + 66.2 ms and t + 67.0 ms. Due to the process complexity, the bubble coalescence and breakup display chaotic behavior. This is due to the chaotic bubble dynamics for the phase change heat transfer, which has been studied extensively previously [16–18]. In fact, the formed elongated bubbles block the channel to increase the pressure drop and reduce the flow rate. Fig. 10 shows the flow patterns for nanofluid. Miniature bubbles are observed, but these bubbles are never merged with each other. Miniature bubbles maintain low pressure drops across the microchannel and good heat transfer performance. The present study identified the non-particles-deposition on the used heater surface. This can be verified

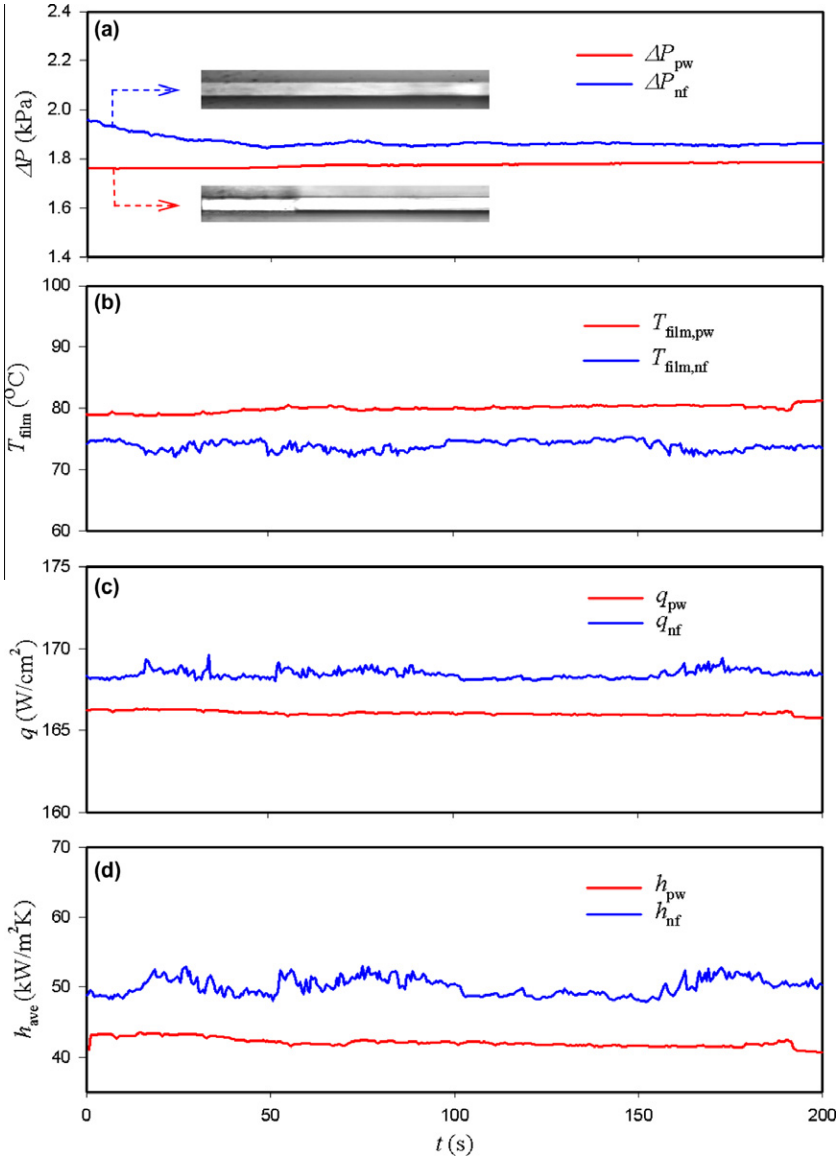

Fig. 7. Various parameters versus time at the point A in Figs. 5 and 6 (T_{in} = 27 °C, T_{out} = 52.6 °C (*pw*), T_{out} = 53.4 °C (*nf*)).

by measuring the contact angles on the fresh non-used heater surface and used heater surface. It is found the contact angle of 36.5° on the used heater surface, which is almost identical to the value of 37.0° on the new clean heater surface.

3.4. Strong unstable boiling for pure water and stable boiling for nanofluids at the point C

Further increase in heat fluxes with the running parameters at the point C (see Figs. 5 and 6) leads to the transient heat transfer shown in Fig. 11. Pressure drops, heater surface temperatures, heat fluxes and heat transfer coefficients display quasi-periodic change versus time for pure water. The unstable boiling flow has large oscillation amplitudes and long cycle periods. For instance, the heater surface temperatures varied in the range of 110–180 °C with the oscillation amplitude of 70 °C. Heat transfer coefficients varied in the range of 50–450 kW/m^{2}K with the oscillation amplitude of 400 kW/m^{2}K. The cycle period is about 200 s. The oscillation with large amplitudes is caused by the flow pattern transition between elongated bubbles and miniature bubbles. The formation of elongated bubble will block the channel, causing the flow rate decrease and pressure drop increase. Thus the heater surface temperatures are increased. Once the formed elongated bubble is expelled out of the channel, fresh liquid comes into the channel and miniature bubbles are generated. Thus the heater surface temperatures are decreased. Fig. 12 shows the transient flow patterns for pure water. The pressure drop decrease stage corresponds to the transition from elongated bubble flow to bubble flow (see images from t to t + 107.367 s in Fig. 12). The pressure drop increase stage corresponds to the transition from bubble flow to elongated bubble flow. The timescale for the flow pattern transition is on the order of 100 s.

For boiling flow with nanofluid, miniature bubbles are maintained to sustain lower and stable heater temperatures compared to pure water. Fig. 13 shows the flow patterns for nanofluid with the running parameters identical to Fig. 11. Due to the high heat flux at the heater surface, elongated bubbles are temporarily observed (see the images at t + 6.4 ms, t + 6.6 ms and t + 6.8 ms), but they are quickly flushed out of the microchannel. Generally the time during which the microchannel is occupied by elongated bubbles is very short and on the order of milliseconds.

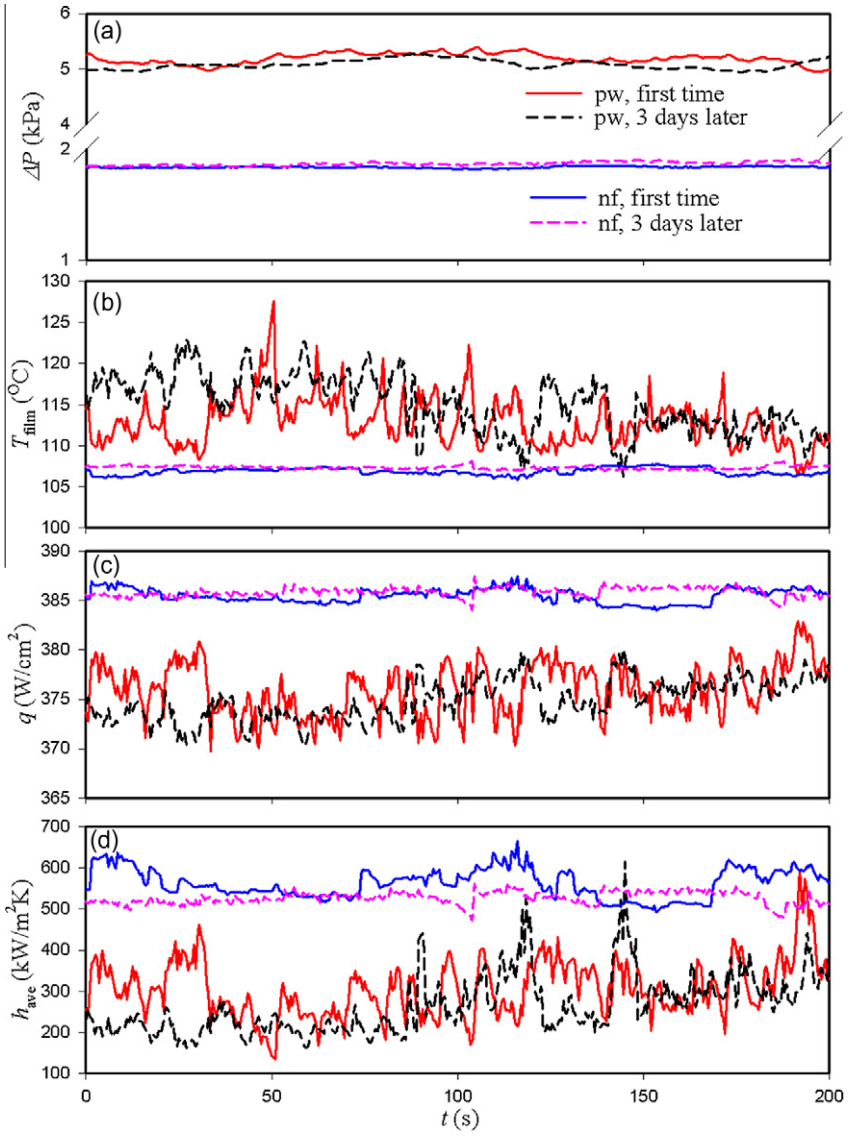

Fig. 8. Various parameters versus time at the point B in Figs. 5 and 6 (T_{in} = 27 °C).

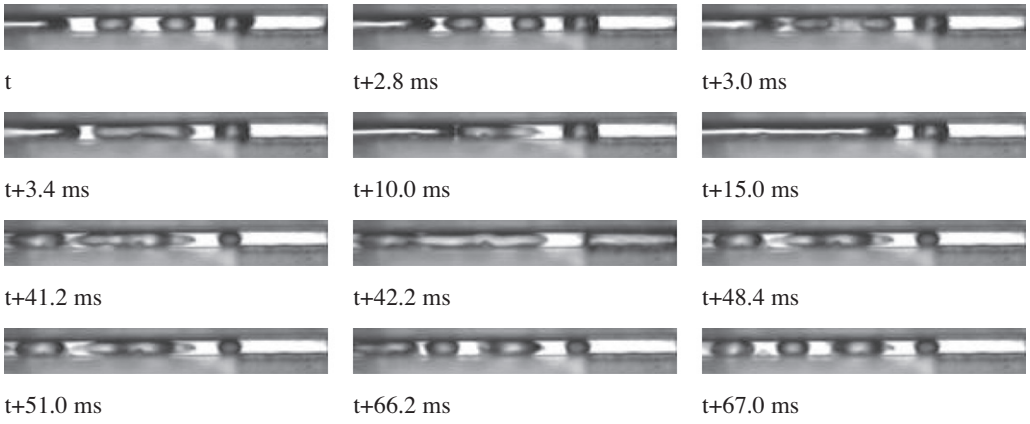

Fig. 9. Coalescence and separation of bubbles for pure water at the point B in Figs. 5 and 6.

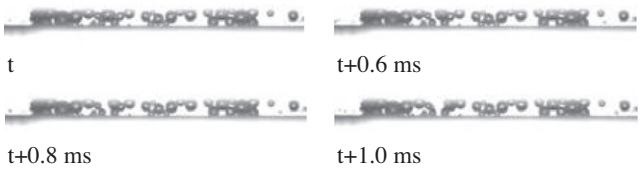

Fig. 10. Miniature bubbles for nanofluid at the point B in Figs. 5 and 6.

3.5. Explanation of the observed flow patterns with and without nanoparticles

Fig. 14a illustrates a bubble growing on the heating surface for pure water. The situation is changed to Fig. 14b for nanofluid. Assuming a uniform heat flux over the heater surface neglecting the slight change of the heat flux versus time, the force balance is written as [19]:

$$p_l - p_v = -\frac{\sigma(d^2H/dx^2)}{[1+(dH/dx)^2]^{3/2}} + \Delta\rho gH + \frac{q^2}{2\rho_v h_{lv}^2} \tag{12}$$

where p is the pressure, l and v represent the liquid and vapor phases, respectively, H is the film thickness, q is the heat flux. The first term of the right hand side is the capillary contribution to the pressure difference, the second term is the gravitational contribution, and the third term is caused by the heating effect. Three heat transfer regions are involved (see Fig. 14a): (1) region I is the area between the heater surface and the dry vapor, (2) region II is the thin liquid film evaporation heat transfer region, and (3) region III is the bulk liquid heat transfer region. It is a common knowledge that there is a thin liquid film beneath the vapor phase for the evaporation heat transfer, that has been described in many references [19–21].

When the system contains nanofluid (see Fig. 14b), the forces applied on the film interface near the solid–liquid–vapor contact line should be modified [22,23]. A structural disjoining pressure should be considered to modify Eq. (12) [19]:

$$p_l - p_v = -\frac{\sigma(d^2H/dx^2)}{[1+(dH/dx)^2]^{3/2}} - \prod(H) + \Delta\rho gH + \frac{q^2}{2\rho_v h_{lv}^2} \tag{13}$$

where $\prod(H)$ is the structural disjoining pressure, pushing the solid-liquid-vapor contact line towards the vapor side to decrease the

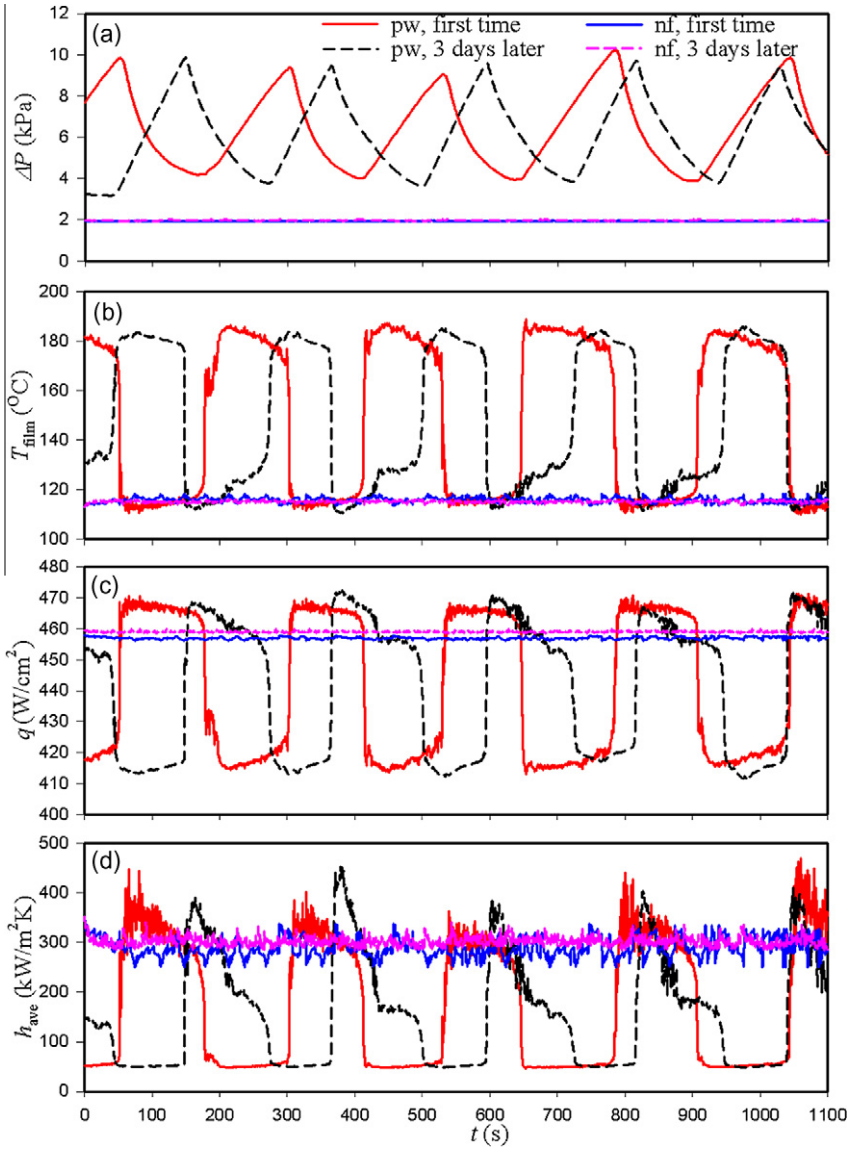

Fig. 11. Various parameters versus time at the point C in Figs. 5 and 6 (T_{in} = 27 °C).

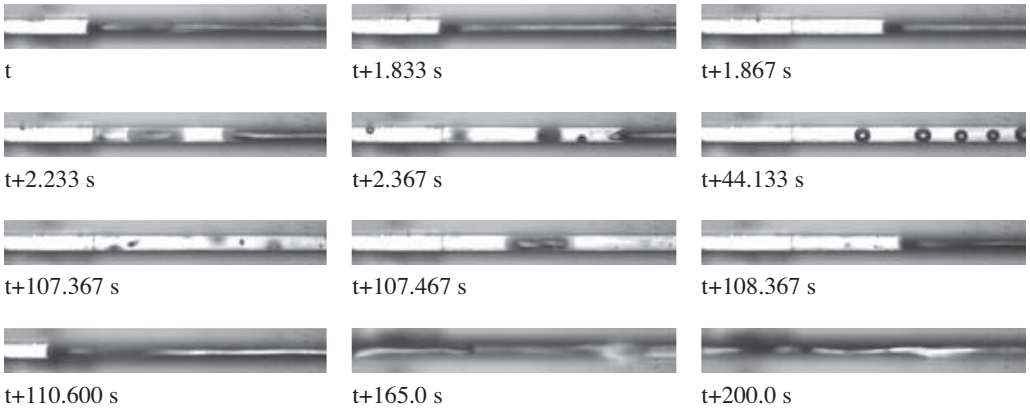

Fig. 12. Flow pattern in the microchannel for pure water at the point C in Figs. 5 and 6.

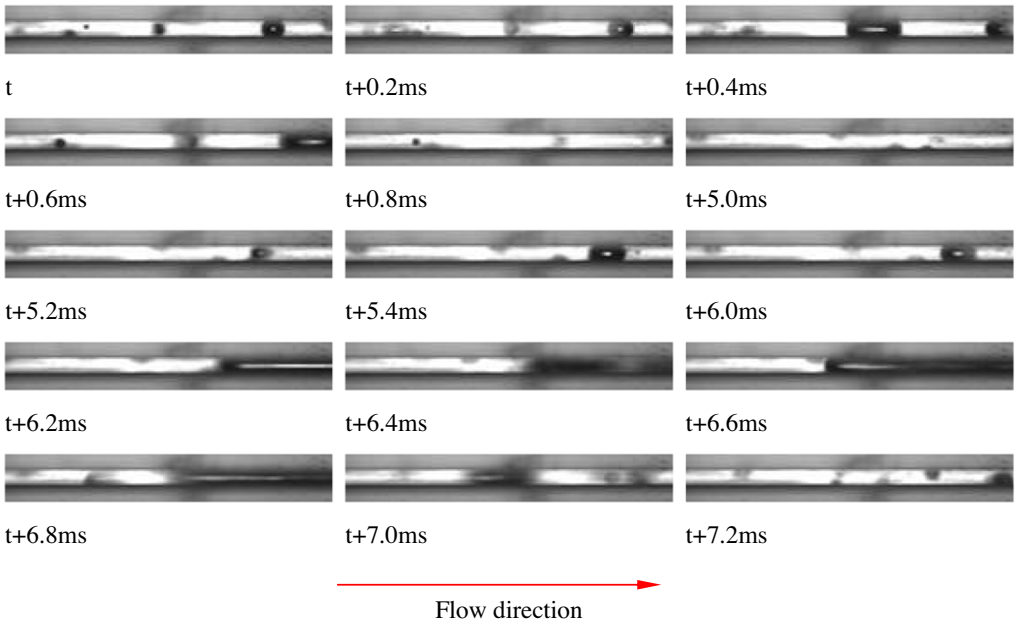

Fig. 13. Flow pattern in the microchannel at the point C in Figs. 5 and 6.

contact area between the heating surface and the dry vapor. Physically, the structural disjoining pressure reflects the molecular forces between nanoparticles and water. It will not occur for pure water because there are no nanoparticles are involved. Fig. 14b shows the four heat transfer regions for nanofluid: (1) region I is the area between the heater surface and the dry vapor, (2) region II is the thin liquid film heat transfer region without nanoparticles involved, (3) region III is the bulk nanofluid region, and (4) region IV is the thin liquid film evaporation heat transfer region with nanoparticles involved. Comparing Fig. 14a and b, nanofluid decreases region I and increases the percentage of the thin liquid film region with nanoparticles involved to the whole bubble shadow area on the heater surface, improving the heat transfer performance for nanofluid.

Based on the classical bubble dynamics theory, the balance among the buoyancy force, surface tension force, drag force and inertia force controls the bubble growth and departure, in which the buoyancy force and drag force cause the bubble departing from the heating surface, but the surface tension force and inertia force prevents the bubble departing from the heating surface. The balance among the four forces are written as (see Fig. 15)

$$\overrightarrow{F_\sigma} + \overrightarrow{F_l} = \overrightarrow{F_g} + \overrightarrow{F_d} \tag{14}$$

During the bubble growing process for pure water, the buoyancy force is increased due to the bubble volume increase. The contact area between the heater surface and the vapor phase is also increased. From the expression $\boldsymbol{F}_\sigma = \sigma D_B \pi \sin\theta$, the surface tension force is increased. Now we consider the nanofluid bubble dynamics. The measured interfacial tension (σ) was 0.072 N/m at the room temperature for nanofluid, which is almost identical to pure water. However, the structural disjoining pressure decreases the diameter D_B for the contact area between the heater surface and the dry vapor (see Fig. 15b), causing the decreased surface tension force on the bubble ($\boldsymbol{F}_\sigma$). This effect decreases the bubble size before the bubble departs, accounting for the miniature bubbles for nanofluid.

Fig. 16 shows the bubble coalescence for pure water. Bubbles shall have larger size before their departure compared to nanofluid. Due to the small channel size considered here, the bubble shall be confined in the channel width direction to form elongated bubble (see Fig. 16a). When the tips of two neighboring bubbles contact with each other, coalescence of the two bubbles begins

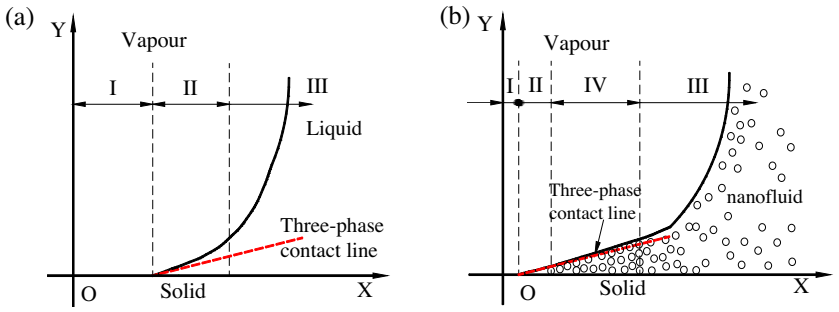

Fig. 14. Solid–liquid–vapor three phase contact line for (a) pure water, and (b) nanofluid.

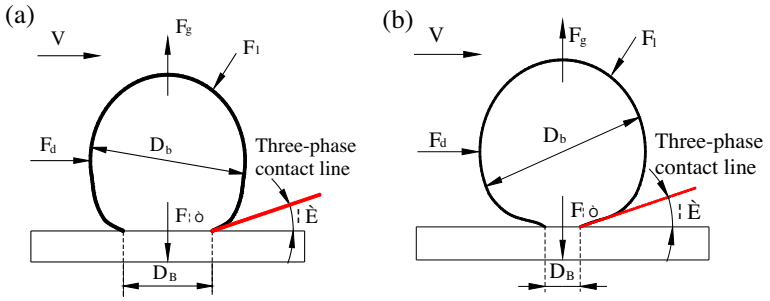

Fig. 15. Force balance acting on the growing bubbles (a) the pure water run and (b) nanofluid run.

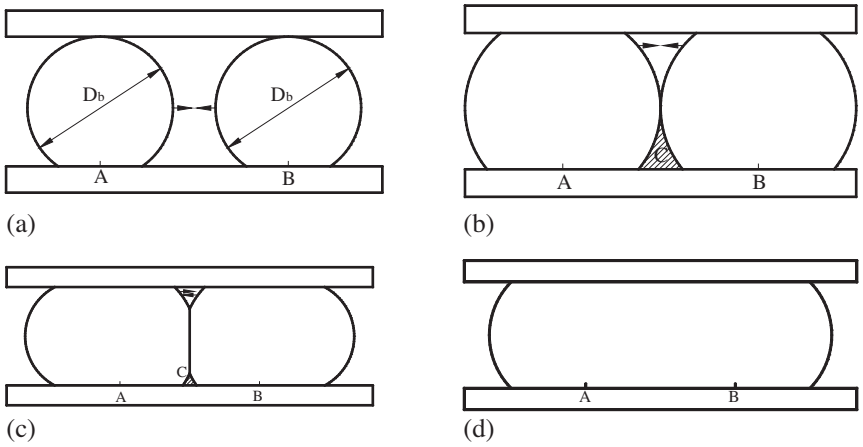

Fig. 16. The merging of the two neighboring bubbles.

(see Fig. 16b). Further growth of the merged bubble decreases the liquids in the two corners (see Fig. 16c). Finally a complete elongated bubble forms, as shown in Fig. 16d. The bubble coalescence and elongated bubble formation process can last 10–100 s for pure water. The bubble coalescence can also take place for nanofluid with short period in the millisecond time scale. The merged bubble will be quickly broken up by the newly formed bubble underneath the long bubble. Thus the flow turns to the miniature bubbles in the channel again.

Fig. 17 shows the idealized picture. The surface tension force ($\boldsymbol{F}_\sigma$) effect on the bubble is decreased, causing the decreased bubble size before its departure. The departure bubble size is smaller than the channel size. This effect leads to the suspended bubbles in the channel. Under the drag force from the flowing stream, the suspended bubbles are flowing along the channel downstream. It is noted that bubble coalescence may also take place for nanofluid at high heat fluxes, but the time at which elongated bubbles exist is short, which is on the order of milliseconds (see Fig. 13). The bubble coalescence for nanofluid in such short timescale does not cause the pressure drop increase, which is different from that for pure water. In summary, elongated bubbles are the main flow pattern for pure water, but miniature bubbles are the main flow pattern for nanofluid.

The flow instability for pure water is strongly related to the flow pattern in the microchannel. Once elongated bubbles appear, they can block the channel, causing the increased pressure drop to reduce the flow rate through the channel. Once the pressure at the microchannel upstream is large enough to push all the elongated bubbles out of the microchannel, the channel is clear and may be occupied by isolated bubble flow. The above process is repeated cycle by cycle, causing the flow instability with large oscillation amplitudes and long cycle periods. On the other hand, the miniature bubbles for nanofluid can not block the channel significantly, maintaining the stable flow and heat transfer.

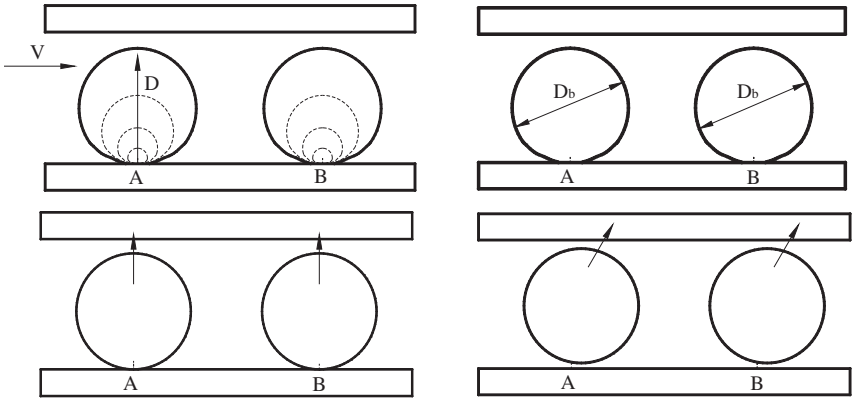

Fig. 17. The bubble departing and flowing downstream of the microchannel before coalescence for nanofluid.

Photo of the microchannel before the experiment

Photo of the microchannel after the experiment

Fig. 18. The microchannel and heating surface before and after the experiments.

3.6. Explanation of the heat transfer behavior with and without nanoparticles

We consider the isolated bubble growth on the heater surface first. There are three heat transfer mechanisms for the boiling heat transfer [24]: (1) the thin liquid film evaporation heat transfer; (2) the heat transfer due to the interchange of the hot and cold liquids during the bubble departure process; (3) the micro convection heat transfer due to the disturbance of the boundary layer during the bubble departure process. We re-take a look at Fig. 14 for the bubble growth on the heater surface for pure water and nanofluid. The following factors account for the heat transfer enhancement by nanofluid: (1) the bubble size before the bubble departure is smaller for nanofluid than that for pure water. This effect causes frequent miniature bubble departure, causing the enhanced heat transfer for the mechanisms due to the interchange of hot and cold liquids, and the micro convection heat transfer by the disturbance of the boundary layer during the bubble departure process, for nanofluid. (2) The dry area for region I is shortened by nanofluid, improving the heat transfer. (3) The percentage of the thin liquid film with nanoparticles to the whole bubble shadow area is increased (region IV, see Fig. 14), enhancing the heat transfer.

As the main flow pattern for pure water, elongated bubbles may block the channel and result in the pressure drop increase. The thin liquid film may be dried out during the channel occupied by elongated bubbles, accounting for the higher heater surface temperatures at this stage. The heat transfer performance is improved once the elongated bubble flow is switched to the isolated bubble flow. For nanofluid, the channel has less possibility to be occupied by elongated bubbles. Isolated miniature bubble majorly contributes to the heat transfer enhancement. For the single-phase liquid flow, the pressure drops are almost identical for both fluids due to the very low nanofluid concentration in this paper (see Fig. 5c–d). Also due to the low nanofluid concentration, the particle deposition on the heater surface was not observed after three weeks operation (see Fig. 18).

It is noted that nanofluid boiling is a very complicated phenomenon. The theory on this topic is not well established at this stage. The structural disjoining pressure can well explain the observed phenomenon here. Alternatively, Das et al. [25] discussed a "surface pressure" regarding nanoparticles as impurities. The surface pressure results from differences of the chemical potential between the impurity and water to reduce the bubble size. Further studies on the nanofluid boiling heat transfer are needed.

4. Conclusions

The boiling heat transfer in a single microchannel with and without nanoparticles was investigated. Compared with other studies, very low nanoparticle concentration of 0.2% was used. Thus particle deposition on the heater surface was not observed. For boiling flow with pure water, boiling heat transfer displays chaotic behavior, caused by the random bubble coalescence and breakup (or separation) in the millisecond timescale. At high heat fluxes, boiling heat transfer behaves oscillations with large amplitudes and long cycle periods. The flow patterns are swicthed between elongated bubbles and miniature bubbles in the timescale of 100 s. The transition from elongated bubble flow to the miniature bubble flow corresponds to the pressure drop decrease stage, and the transition from miniature bubble flow to elongated bubble flow corresponds to the pressure drop increase stage. Nanofluid stabilizes the boiling flow. Miniature bubbles are continuously sustained in the microchannel. Besides, nanofluid inhibits the dry patch development between the heater surface and the vapor phase. The increased percentage of the thin liquid film evaporation heat transfer accounts for the heat transfer enhancement with nanofluid. The present work identifies a possibility that nanofluid with low concentrations can be used in forced convective boiling heat transfer with microchannel test sections.

Acknowledgements

The authors thank for the financial support by the National Natural Science Foundation of China with the contract numbers of U1034004 and 50825603, the National Basic Research Program with the contract number of 2011CB710703, the Beijing Science and Technology Program (Z111109055311097) and the Suzhou industry project (SYG201105).

References

[1] S.U.S. Choi, Enhancing thermal conductivity of fluids with nanoparticle, ASME FED 231 (1995) 99–105.
[2] X.Q. Wang, A.S. Mujumdar, Heat transfer characteristics of nanofluids: a review, Int. J. Therm. Sci. 46 (2007) 1–19.
[3] D. Weerapun, W. Somchai, A critical review of convective heat transfer of nanofluids, Renew. Sust. Energ. Rev. 11 (2007) 797–817.
[4] D.S. Wen, G. Lin, S. Vafaei, K. Zhang, Review of nanofluids for heat transfer applications, Particuology 7 (2009) 141–150.

[5] J.A. Eastman, S.U.S. Choi, Anomalously increased effective thermal conductivities of ethylene glycol-based nanofluids containing copper nanoparticles, Appl. Phys. Lett. 78 (2001) 718720.
[6] S.J. Kim, T. McKrell, J. Buongiorno, L.W. Hu, Experimental study of flow critical heat flux in alumina-water, zinc-oxide-water, and diamond-water nanofluids, J. Heat Trans. 131 (2009) 043204–043211.
[7] S.J. Kim, T. McKrell, J. Buongiorno, L.W. Hu, Subcooled flow boiling heat transfer of dilute alumina, zinc oxide, and diamond nanofluids at atmospheric pressure, Nucl. Eng. Des. 240 (2010) 1186–1194.
[8] H.S. Ahn, H. Kim, H.J. Jo, S.H. Kang, W.P. Chang, M.H. Kim, Experimental study of critical heat flux enhancement during forced convective flow boiling of nanofluid on a short heated surface, Int. J. Multiphase Flow 36 (2010) 375–384.
[9] S.K. Das, N. Putra, W. Roetzel, Pool boiling characteristics of nano-fluids, Int. J. Heat Mass Transfer 46 (2003) 851–862.
[10] S.M. Kwark, G. Moreno, R. Kumar, H. Moon, S.M. You, Nanocoating characterization in pool boiling heat transfer of pure water, Int. J. Heat Mass Transfer 53 (2010) 4579–4587.
[11] H.S. Ahn, S.H. Kang, M.H. Kim, Visualized effect of alumina nanoparticles surface deposition on water flow boiling heat transfer, Exp. Therm. Fluid Sci. 37 (2012) 154–163.
[12] J. Lee, I. Mudawar, Assessment of the effectiveness of nanofluids for single-phase and two-phase heat transfer in micro-channels, Int. J. Heat Mass Transfer 50 (2007) 452–463.
[13] H. Peng, G. Ding, W. Jiang, H. Hu, Y. Gao, Heat transfer characteristics of refrigerant-based nanofluid flow boiling inside a horizontal smooth tube, Int J. Refrig. 32 (2009) 1259–1270.
[14] K. Henderson, Y.G. Park, L. Liu, A.M. Jacobi, Flow-boiling heat transfer of R-134a-based nanofluids in a horizontal tube, Int J. Heat Mass Transfer 53 (2010) 944–951.
[15] J.P. Holman, Experimental Methods for Engineers, fourth ed., McGraw-Hill, NY, 1984.
[16] G.D. Wang, P. Cheng, An experimental study of flow boiling instability in a single microchannel, Int. Comm. Heat Mass Transfer 35 (2008) 1229–1234.
[17] H.Y. Wu, P. Cheng, Boiling instability in parallel silicon microchannels at different heat flux, Int. J. Heat Mass Transfer 47 (2004) 3631–3641.
[18] J.L. Xu, G.H. Liu, W. Zhang, Q. Li, B. Wang, Seed bubble stabilize flow and heat transfer in parallel microchannels, Int. J. Multiphase Flow 35 (2009) 773–790.
[19] D.S. Wen, Mechanisms of thermal nanofluids on enhanced critical heat flux (CHF), Int. J. Heat Mass Transfer 51 (2008) 4958–4965.
[20] J.R. Thome, V. Dupont, A.M. Jacobi, Heat transfer model for evaporation in microchannels. Part I: presentation of the model, Int. J. Heat Mass Transfer 47 (2004) 3375–3385.
[21] L.P. Yarin, A. Mosyak, G. Hetsroni, Fluid Flow, Heat Transfer and Boiling in Micro-Channels, Springer, 2009.
[22] D.T. Wasan, A.D. Hikolov, Spreading of nanofluids on solids, Nature 423 (2001) 156–159.
[23] A. Chengara, A.D. Nikolov, D.T. Wasan, A. Trokhymchuk, D. Henderson, Spreading of nanofluidsdriven by the structural disjoining pressure gradient, J. Colloid Interf. Sci. 280 (2004) 192–201.
[24] C.E. Brennen, Fundamentals of Multiphase Flow, Cambridge University Press, UK, 2005. 150–162.
[25] S. Das, J.H. Snoeijer, D. Lohse, Effect of impurities in description of surface nanobubbles, Phys. Rev. E 82 (2010) 056310.